Aerosol Science and Technology

ISSN: 0278-6826 (Print) 1521-7388 (Online) Journal homepage: https://www.tandfonline.com/loi/uast20

Measurements of Kinetic Energy Loss for Particles Impacting Surfaces

Stephen Wall , Walter John , Hwa-Chi Wang & Simon L. Goren

To cite this article: Stephen Wall , Walter John , Hwa-Chi Wang & Simon L. Goren (1990) Measurements of Kinetic Energy Loss for Particles Impacting Surfaces, Aerosol Science and Technology, 12:4, 926-946, DOI: 10.1080/02786829008959404

To link to this article: https://doi.org/10.1080/02786829008959404

Measurements of Kinetic Energy Loss for Particles Impacting Surfaces

Stephen Wall, Walter John, and Hwa-Chi Wang
Air and Industrial Hygiene Laboratory, California Department of Health Services, Berkeley, CA 94704

Simon L. Goren
Department of Chemical Engineering, University of California, Berkeley, Berkeley, CA 94720

Incoming and rebounding particle velocities were measured to within several particle diameters of the impaction surface using laser Doppler velocimetry. Impacts occurred normal to the surface and ranged from 1 m/s, near the threshold for particle bounce, to 100 m/s, well into the plastic damage regime. Monodisperse ammonium fluorescein spheres, 2.6–6.9 μm in diameter, impacted target surfaces including polished molybdenum and silicon, cleaved mica, and a fluorocarbon polymer. The incident kinetic energy recovered on rebound depended on particle size and target composition at low velocity (< 20 m/s), where the adhesion surface energy is important. No dependence on target composition was found at higher velocities where up to half of the impact energy was lost to plastic deformation. Plastic deformation was a significant component of energy loss even at impact velocities near critical velocity. Critical velocities for the onset of bounce decreased with a stronger power-law dependence on particle diameter than expected from classical adhesion theory or the elastic flattening model proposed by Dahneke. This is consistent with kinetic energy loss contributions from both plastic deformation and surface forces. Auxiliary experiments conducted with and without continuous discharge of the impact surface indicated the absence of a significant electrostatic contribution to particle adhesion.

INTRODUCTION

The capture of particles on impact with a surface is a fundamentally important step in aerosol collection and in natural deposition processes, but remains an incompletely understood phenomenon. Particles are known to escape collection and rebound from surfaces when the impact velocity exceeds a characteristic critical velocity, which is determined by the particle size and the materials involved. For many materials, the yield pressure above which plastic deformation begins is exceeded even at the relatively low velocities near the critical velocity. To achieve a fundamental understanding of the adhesion process occurring during particle impacts requires the measurement of the kinetic energy loss over a wide range of velocities, particle size, and materials so that the effects of plastic deformation as well as adhesion can be taken into account.

The current study was undertaken to further the understanding of particle bounce processes, including adhesion and plastic deformation, through direct measurements of incident and rebounding particle velocities. Freshly generated, monosized solid particles were impacted on several different well-characterized surfaces. The particle size dependence of critical velocity was investigated. The change in energy loss with particle velocity and target material was also investigated.

0278-6826/90/$3.50
Aerosol Science and Technology 12:926–946 (1990)

PREVIOUS WORK

Dahneke (1972) considered surface adhesion arising from elastic deformations, but energy loss mechanisms were not specified in any detail. Brenner et al. (1981) considered plastic deformation for large metal particle impacts. Rogers and Reed (1984) first considered both elastic and plastic deformations occurring during large particle-surface impacts. However, the experimental data currently available for particles of micrometer size are inadequate to test these theories.

Previous experimental measurements of adhesion for particles impacting surfaces have used two different basic approaches. In the first, the onset of particle bounce from a surface is detected as a decrease in collection efficiency which occurs at sufficiently high impact velocity. The particle velocity is not determined directly, but is estimated from a calculated flowfield. This basic approach was applied by Esmen et al. (1978), D'Ottavio and Goren (1983), Aylor and Ferrandino (1985) and Wang and John (1988).

In the second experimental approach, direct measurements are made of the incoming and rebounding particle velocities. Dahneke (1973) first used this approach in vacuum to determine that polymer particles impacting smooth hard targets suffer up to a 20% loss in kinetic energy. Unfortunately, limitations of the bounce cell design prevented measurements down to near-critical velocity, where energy loss owing to surface adhesion dominates. High-speed photography was used by Broom (1979), Hiller and Löffler (1980), and Paw U (1982), to determine particle trajectories close to the surface. Paw U, using biological particles impacting natural leaf surfaces, and Broom, using glass microspheres and unpolished metal targets, found the inherent surface roughness of these materials to have a major effect on particle rebound. This may be due to plastic deformation of surface asperities. Hiller and Löffler discussed the importance of plastic deformation as an energy loss mechanism in the impacts of smooth, solid particles with a small fiber, but a detailed model was not developed.

Most recently, Rogers and Reed (1984) investigated impacts for large (15–40 μm) copper microspheres in order to evaluate an elastic-plastic impact model for particle adhesion. Critical impact velocities at the surface were obtained directly with a high speed camera for those particles which just failed to rebound. Application of the model provided an estimate of adhesion energy at the particle–surface interface in general agreement with independent determinations of surface energy from liquid contact angle measurements. However, there was significant uncertainty in the comparison because the sizes of the test particles were not accurately known.

THEORETICAL BACKGROUND

A schematic diagram of the particle bounce process treated as a simple energy balance is shown in Figure 1. An energy balance for the impact is $K_i + E_i - K_L = K_r + E_r$ and rebound occurs for $K_e > E_r$, where K_i and K_r are the kinetic energy for the incoming and rebounding particle, E_i and E_r are the potential energy of interaction with the surface for the incoming and rebounding particle, and K_L is the energy loss during the impact. The fraction of the impact energy recovered in terms of the incoming velocity V_i and the rebounding velocity V_r is:

$$V_r^2/V_i^2 = e^2 + 2\,\Delta E/MV_i^2, \qquad (1)$$

where $\Delta E = E_i - E_r$ and the coefficient of restitution, $e = (1 - K_L/K_i)^{1/2}$. Here the classical definition of e is used in contrast to the form used by Dahneke, $e = (1 - K_L/(K_i + E_i))^{1/2}$, which does not reduce to the classical form even when $\Delta E = 0$. The classical definition does not assume e and E_i to be mutually independent parameters, which is important since both may be re-

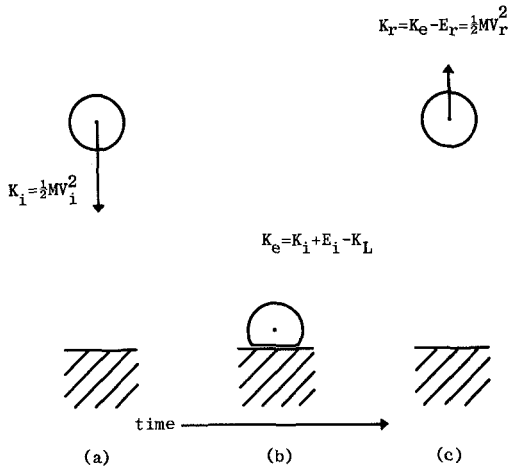

FIGURE 1. A diagram of the particle bounce process as a simple energy balance for normal impacts showing (*a*) the incoming particle approaching the surface (*b*) the particle at full compression before rebound, and (*c*) the rebounding particle.

lated to the amount of material deformation on impact.

The critical velocity for particle capture is:

$$V_i^* = \left(-2\,\Delta E/(Me^2)\right)^{1/2}. \tag{2}$$

The well-known Hertz equations for purely elastic impacts and the elastic yield limit Y of the material can be utilized to determine the limiting velocity V_y, above which plastic deformation begins to occur. As can be shown from Bitter (1963):

$$V_y = (2\pi/3K)^2(2/5\rho)^{1/2}Y^{5/2}, \tag{3}$$

where ρ is the density of the particle and the mechanical constant $K = 4/3(\kappa_1 + \kappa_2)$ with $\kappa_i = (1 - \nu_i^2)/\xi_i$, where ν_i is the Poisson ratio and ξ_i is Young's modulus for the material of object i. The limiting velocity is determined by the bulk material properties and is independent of particle size. As an example, the bulk properties of polystyrene are known to be $\kappa = 2.75 \times 10^{-10}$ m^2/N, $\rho = 1.05 \times 10^3$ kg/m^3, and $Y = 4.8 \times 10^7$ N/m^2. For polystyrene microspheres impacting a hard target, as investigated by Dahneke (1973) and also Cheng and Yeh (1979), plastic damage would be expected to occur for impact velocities as small as 0.06 m/s. This is more than an order of magnitude lower than the critical velocities reported by these researchers.

The elastic energy stored in a particle-surface impact before plastic deformation begins is just the limiting kinetic energy, $K_y = MV_y^2/2$. An expression derived by Bitter (1963) for the impact energy loss due to plastic deformation, K_p, can be expressed as:

$$K_p = \left[(K_i - K_y/16)^{1/2} - (15K_y/16)^{1/2}\right]^2. \tag{4}$$

From energy conservation, Rogers and Reed (1984) determined the necessary condition for particle rebound on impact with a surface to be:

$$K_i - K_p > E_a, \tag{5}$$

where $(K_i - K_p)$ is the stored elastic energy available for rebound, and E_a is the total adhesion energy derived from the equilibrium circle of contact. The total adhesion energy at equilibrium has been shown by Johnson et al. (1971) to be the sum of two energy terms:

$$E_a = E_m + E_s, \tag{6}$$

which are expressed here in terms of the forces F_o, F_s, and F_m for convenience.

F_o, the externally applied load, was considered to be the gravitational force due to the mass of the particle. This force is augmented by the surface forces F_s to yield a total applied load F_t:

$$F_t = F_o + 2F_s + 2\left[F_sF_o + F_s^2\right]^{1/2}, \tag{7}$$

where

$$F_s = 3/2\,\Delta\gamma\,\pi r_t^3(K/F_m), \tag{8}$$

$\Delta\gamma$ is the adhesion surface energy per unit area, and r_t is the total projected radius of contact without surface forces for a particle of radius R, as derived from Rogers and

Reed (1984),

$$r_t = \left(r_e^2 + r_p^2\right)^{1/2}.$$

Here $r_e = (5K_y R^2/2K)^{1/5}$ is the maximum contact circle radius under purely elastic compression and,

$$r_p = 3K\left[(15/16)K_y K_p\right]^{1/4}/\left[(\pi Y)^{3/2}R^{1/2}\right]$$

is the radius of the plastic deformation contact circle, which forms at the center of contact upon further compression after the yield limit is reached. The total mechanical force F_m exerted in producing the elastic deformation in the particle is the sum of the force in the elastic region,

$$F_e = (R^{1/2}K)^{2/5}(5K_y/2)^{3/5},$$

derived by evaluating the Hertz law (Timoshenko and Goodier, 1951) at the elastic limit velocity, and the elastic force in the plastic region, $F_p = \pi r_p^2 Y$.

The mechanical potential energy due to the surface contact is then

$$E_m = F_o F_m^{1/3}\left[\left(F_t^{2/3} + 2F_o F_t^{-1/3}\right)/3Kr_t\right], \quad (9)$$

and the surface energy developed over the interfacial contact is

$$E_s = \Delta\gamma\,\pi r_t^2 (F_t/F_m)^{2/3}, \quad (10)$$

where the term $(F_t/F_m)^{2/3}$ can be considered a contact area enhancement factor introduced by the action of the adhesion forces at the interface.

In the Rogers and Reed model, plastic deformation occurs in the central region of the circle of contact and is surrounded by an annular region of elastic deformation. A similar model for elastic-plastic impacts was subsequently proposed by Fichman and Pnueli (1985), who added a second region of plastic deformation at the circumference of the contact circle where the material is under tension. In order to apply the model of Fichman and Pnueli, corrections to several of their equations are necessary as pointed out by Reed (1986), as well as, a proper integration of the expression for the energy loss to plastic deformation at the contact perimeter.

EXPERIMENTAL SYSTEM AND PROCEDURES

Approach

Measurements of bounce normal to the surface were made to determine the particle energy loss on impact with a solid surface. The particles were freshly generated, solid, monodisperse spheres of ammonium fluorescein of 3–7 μm in diameter. The impaction surfaces were molybdenum, silicon, mica, and Tedlar. Kinetic energy loss was determined by measuring the particle velocities before and after impact by laser Doppler velocimetry. Since the particles decelerate under the aerodynamic drag force, velocity measurements were made as close as 10 μm from the surface to minimize extrapolation to the values at impact. Impact velocities were varied from 1 to 100 m/s, which encompassed the adhesion dominated regime at near-critical velocity up to the plastic damage dominated regime at high velocity. In order to reach the lowest particle impact velocities, second bounces were utilized.

Experimental Arrangement

The experimental system arrangement is shown in Figure 2. Highly monodisperse ammonium fluorescein particles were produced by a vibrating-orifice aerosol generator. The solution drops dried in 30% RH dilution air to form solid, nonhygroscopic spheres with featureless surfaces as reported by Vanderpool and Rubow (1984). High-magnification electron microscopy analysis indicated the surface to be smooth down to near-molecular scale (3 nm). Calculation of the particle size from the vibration frequency, solution feedrate and concentration has been shown to be highly accurate (Wall et al., 1985). In the present study the particle diameters were estimated to be accurate to $\pm 1\%$. The geometric particle diameters used in this study were 2.58, 3.44, 4.90, and 6.89 μm. Particle size and

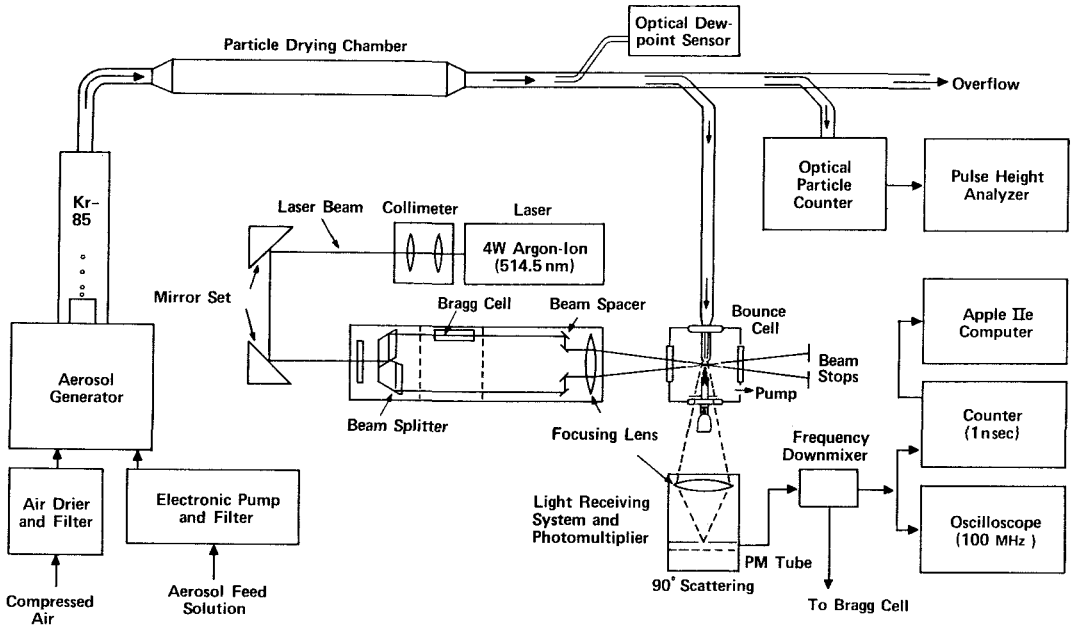

FIGURE 2. Schematic representation of the experimental system including the particle generator, the laser Doppler velocimeter, and the bounce cell. The light receiving system is actually normal to the plane of the figure.

monodispersity were continuously monitored with an optical counter (Climet 208) and a pulse height analyzer. Particle density, as measured by the microscopy technique of John and Wall (1983), was $1.35 \pm 0.02 \times 10^3$ kg/m^3 and independent of particle size. The aerosol passed through a ^{85}Kr source to reduce particle charge to the Boltzmann equilibrium distribution before entering the bounce cell.

Incoming and rebounding particle velocity measurements were made with the dual beam laser Doppler system as shown. The 4-W argon ion laser was operated to produce a 350-mW beam at the primary emission wavelength of 514.5 nm. Two parallel beams were produced with a beam splitter and brought to a 126-μm diameter focus inside the bounce cell with a 210-mm transmission lens. The velocity measurement volume was defined by the fringe pattern (14.88-μm spacing) created in the beam crossover zone above the impact target. A 90° light-scattering geometry was used, since by imaging the photomultiplier aperture into the long cylindrical fringe region at the beam crossing, the length of the measuring volume was reduced to 126 μm. Also, light scattering from the target could be minimized. Particles crossing the interference fringes produced a Doppler signal with a frequency proportional to velocity.

Bounce Cell

A cross sectional view of the particle bounce cell is shown in Figure 3*a*. Particles were accelerated in a nozzle (1016-μm diameter, 102-μm length) from the TSI aerodynamic particle sizer which is designed to operate at velocities near 150 m/s. The velocity range of interest here was from 1 to 100 m/s. At the smaller pressure drops required for these lower velocities, the reduced proportion of sheath air resulted in large radial gradients in particle velocity. A

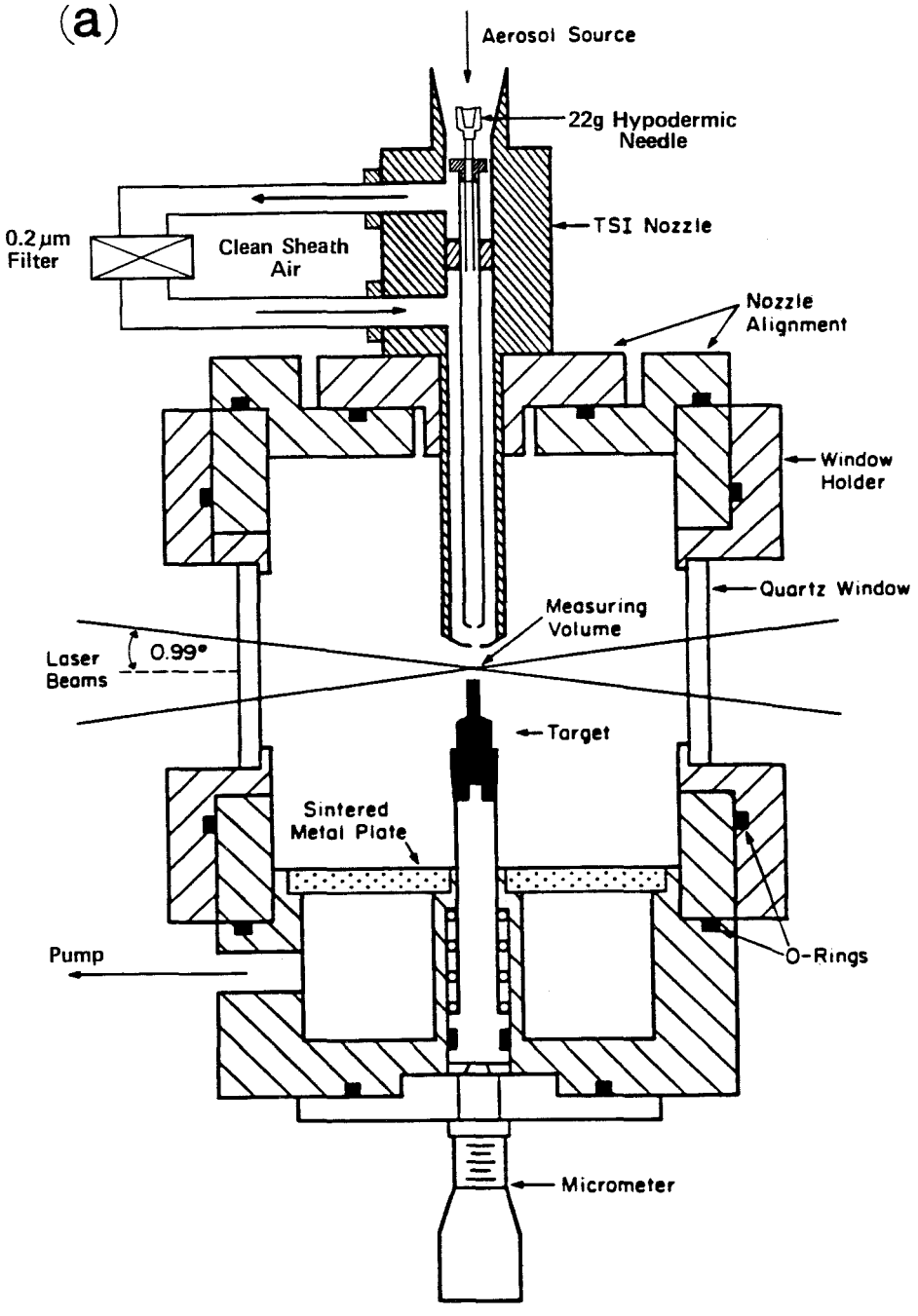

FIGURE 3. (*a*) Cross section of the bounce cell showing the particle acceleration nozzle, impaction target, and laser beams. (*b*) Enlargement of the particle velocity measurement region showing the components to scale.

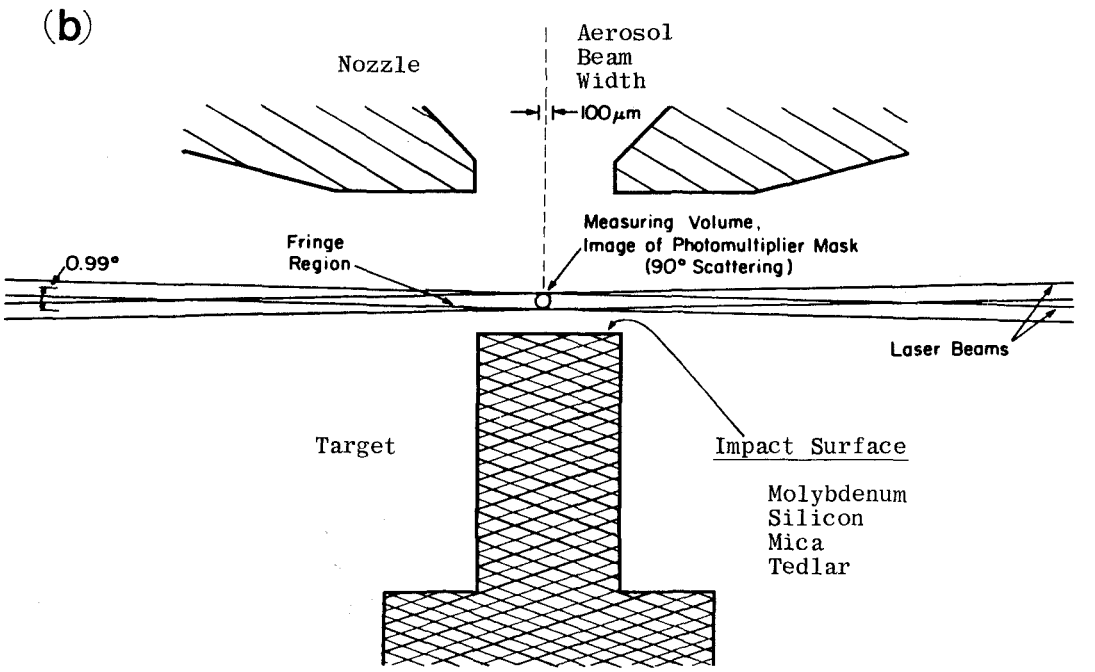

FIGURE 3. (Continued).

22-gauge (600 μm I.D.) hypodermic needle was installed in the aerosol nozzle inlet to reestablish the sheath-to-aerosol flow rate design ratio of 4. This produced a particle beam less than 100 μm in diameter having a velocity profile flat to within 5%. The nozzle was aligned coaxially with the target by sighting down the nozzle with a telescope and also through the PM tube collection optics with a cross-hair alignment eyepiece.

In order to bring the measuring volume close to the impaction surface, a small inter-beam half-angle of 0.99° was necessary, as shown to scale in Figure 3*b*. The use of impaction targets with diameters comparable to the 1000-μm aerosol acceleration nozzle size avoided blockage of the lower laser beam by the front edge of the target. This allowed measurements to be made less than 10 μm from the impaction surface. A nozzle-to-target distance of between 1300 and 1500 μm was used for all measurements. The bounce cell was moved as a rigid unit by three orthogonal, precision (± 1 μm) motorized micrometers (Oriel motormike) to change the measurement location above the impaction surface.

Impaction Surfaces

Particle impaction targets included molybdenum and silicon, hard materials with surface roughness determined by a high mechanical polish, muscovite mica, cleaved to obtain a molecularly smooth surface, and Tedlar, a deformable fluorocarbon polymer cast as a thick film. The molybdenum target was machined from pure stock using only distilled water as a lubricant and the impaction surface was hand-polished using successively finer 400–1200-mesh silicon carbide particles, embedded in an elastomer backing (Micromesh MX) to prevent gouging. The impaction surface flatness and sharp edge were maintained during polish-

ing by keeping the target surface flush with a surrounding cylinder of the same stock.

The silicon target was cut from an electronics-grade, single crystal wafer to preserve the high polish received during manufacture. To avoid straining the crystal, the wafer was cut in a precision drill press by slowly rotating a hardened metal tube coated at the edge with polishing compound. As with the molybdenum target, the silicon surface was carefully cleaned by flooding with reagent grade isopropyl alcohol.

The natural muscovite mica target was custom machined from optical-grade material by the supplier (Spruce Pine Mica) to avoid delamination of the crystal layers. Before use, the mica was cleaved by hand to yield a fresh surface.

The Tedlar target was punched from a 50-μm-thick foil after the backside surface had been glued to the edge of a stainless steel mounting ring for support. Examination under a polarized light microscope confirmed the absence of residual strain in the target bulk material. A separate Tedlar target was also prepared with a thin gold coating (8.3 nm thick) applied by vacuum evaporation to make the surface conducting. Complete adhesion of the gold film was achieved only after cleaning the Tedlar surface by ultrasonication in acetone followed by exposure to an ion plasma just prior to coating.

Examination for *macroscale* roughness by scanning electron microscopy indicated the silicon surface to be as featureless as mica within the 0.1-μm resolution of the instrument. Both molybdenum and Tedlar were relatively smooth surfaces, but were found to have detectable macroscale roughness with up to 0.3-μm asperities. The *microscale* roughness of the molybdenum target was also measured with a laser interferometer (Wyco) and found to be < 5.0 nm as compared with 0.5 nm for the best polished metal standards. Electron micrographs of the target surfaces as well as the surface of the ammonium fluorescein particles are shown in Figure 4.

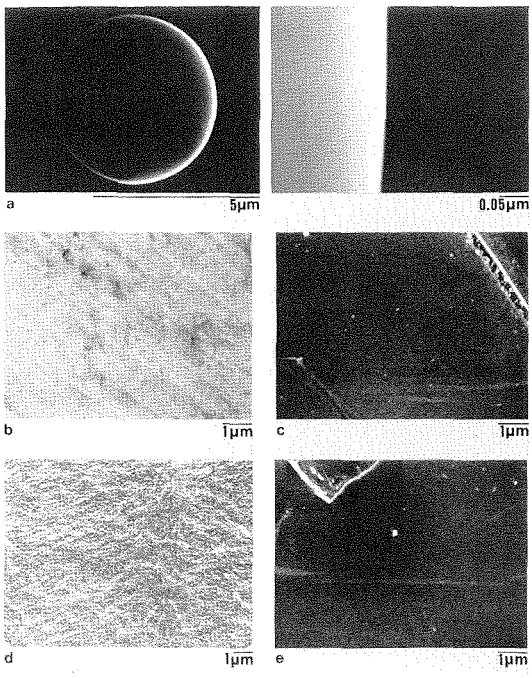

FIGURE 4. High-magnification electron micrograph showing the surfaces of the (*a*) ammonium fluorescein particles at both low and high magnification, (*b*) molybdenum target, (*c*) silicon target, (*d*) Tedlar target, and (*e*) mica target. The surface defects shown in *c* and *e* were rare and are included here only to provide contrast with an otherwise featureless surface.

Doppler Signal Processing

A Bragg cell was used to continuously shift the fringe pattern toward the surface in order to distinguish the direction of particle motion and to improve spatial resolution of the velocity measurement (Drain, 1972). Fringe shifting towards the surface was preferred because the particles rebound with a velocity lower than the incident velocity. The Doppler signal from the photomultiplier tube was processed with a high speed counter (TSI model 1990 B) to yield particle velocities.

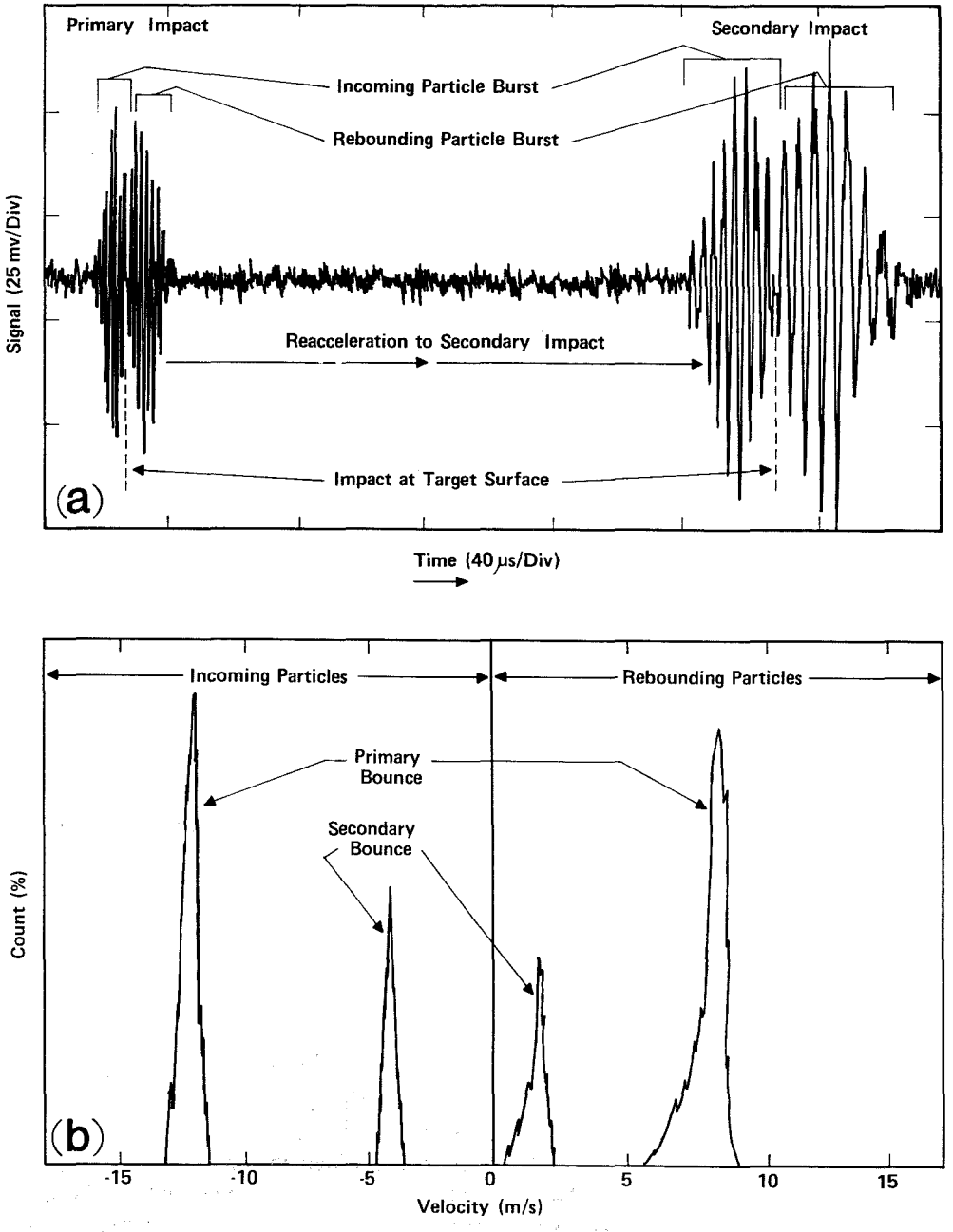

FIGURE 5. (*a*) Typical Doppler burst sequence close to the target showing initial impact and secondary impact after reacceleration. (*b*) Example of incoming and rebounding velocity distributions accumulated for over 250 primary and secondary impacts.

A typical near-surface Doppler burst for a single particle *after* shaping by the counter is illustrated in Figure 5*a*. As indicated in the figure, it was possible to detect the initial incoming velocity and rebounding velocity (first bounce) as well as a secondary incoming and rebounding velocity (second bounce) due to the reacceleration toward the target of the initially rebounding particle. In this example the fringes are so close to the impaction surface that the incoming and rebounding Doppler bursts appear to merge at the point of particle contact with the surface.

Individual particle velocity measurements from the counter were acquired and stored by an Apple IIe computer through the standard interface board (TSI model 1992). Because of the slow processing speed of the computer (75 μs/data point), incoming and rebounding velocities for the *same* particle could not be recorded even though the information was in the signal (Figure 5*a*). Instead, each of the incoming and rebounding velocities reported here represent mean values computed from more than 250 individual measurements. An example of a typical velocity distribution for multiple bounces on a molybdenum target is shown in Figure 5*b*. In general, the peaks in the distribution were sufficiently sharp to yield a relative standard deviation of $< 10\%$ and sufficiently symmetric to give a calculated mean velocity near the mode. A small skew toward lower velocities can be seen (Figure 5*b*) in the rebounding distributions only. This effect was nearly absent for the molecularly smooth mica target. The degree of skew increased for the targets in the order mica, silicon, Tedlar, and molybdenum, which is in the order of increasing surface roughness.

The determination of the precise distance above the target surface where the velocity was measured, Z_p, required development of the model shown in Figure 6. To determine the midpoint Z_m of the measuring volume, a 5-μm diameter glass fiber was placed on the impaction surface normal to the axis of the laser beam and moved vertically with the z-axis digital micrometer thereby generating a Doppler burst count rate profile. The maximum Doppler burst count rate was used to establish the midpoint of the measuring volume.

The diameter of the effective measuring volume D_m for the ammonium fluorescein particles was evaluated, under the conditions of the data collection, by calculating the product of the time the oscilloscope trace of the burst exceeded the counter threshold level and the mean particle velocity. D_m could not be determined in advance using the target mounted fiber, since the

FIGURE 6. Model employed to determine the distance above the impact surface where the particle velocity is measured.

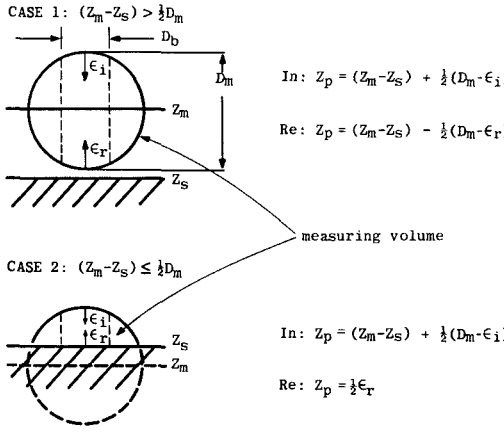

Where:

Z_m = midpoint of the measuring volume

Z_s = location of the impaction surface

Z_p = distance above the surface where particle velocity is measured

$\epsilon_{i,r}$ = distance particle moves to cross the required number of fringes N_a, to generate a velocity measurement

$= N_a D_f \left(\frac{f_p}{f_s \pm f_p}\right)$; + rebound, - incoming

f_p = Doppler frequency due to particle velocity (MHz)

f_s = fringe shift frequency (10MHz)

D_f = fringe spacing (14.88μm)

D_b = Diameter of the particle beam (90% count probability)

effective measurement volume diameter changes with light scattering characteristics and the counter threshold. Measurements of the surface location and measurement volume size were reproducible within 10 μm.

Particles must travel a distance ϵ (Figure 6) into the measuring volume in order to cross a sufficient number of fringes for a velocity measurement. The midpoint of ϵ was used as the measurement location with a position uncertainty of $1/2\ \epsilon$. Typically ϵ was $< 20\ \mu$m and decreased to $< 2\ \mu$m for the lowest velocities measured. The diameter of the particle beam, indicated in Figure 6 as D_b, was sufficiently narrow ($\simeq 60\ \mu$m) that little error was introduced in the calculation of velocity measurement position by assuming that all particles entered the measuring volume along the centerline.

Particle Trajectory Analysis

For each fixed acceleration nozzle flow rate, measurements of mean incoming and rebounding particle velocities were made as a function of distance above the impaction surface along the particle beam centerline. The five particle sizes of 0.516, 2.58, 3.44, 4.90, and 6.89 μm in geometric diameter were employed for each target material. The 0.516-μm particle size was utilized as a flowfield tracer to establish the centerline gas velocity. To extrapolate these velocities to impact, particle trajectories were calculated from an equation of particle motion using 5th order Runge-Kutta numerical integration. The nondimensional form of the equation of particle motion used was:

$$Stk^{\circ}(dV_p^*/dt^*) = \left[1 + 0.158 Re_p^{o2/3}(V_g^* - V_p^*)^{2/3}\right] \times (V_g^* - V_p^*), \quad (11)$$

where $V_g^* = V_g/V_g^{\circ}$ is the initially unknown nondimensional gas velocity, $V_p^* = V_p/V_g^{\circ}$ is the nondimensional particle velocity, $dV_p^*/dt^* = (a/V_g^{o2})dV_p/dt$ is the nondimensional particle acceleration, V_g° is the gas velocity measured at the nozzle using 0.516-μm particles, and a is the nozzle radius. Stk°, the particle Stokes number at the nozzle, is defined as:

$$Stk^{\circ} = \rho_p d_p^2 C_s V_g^{\circ}/(18\mu a). \quad (12)$$

The initial particle Reynolds number, Re_p°, is defined as:

$$Re_p^{\circ} = \rho_g d_p V_g^{\circ}/\mu, \quad (13)$$

where ρ_p and ρ_g are the particle and gas densities, d_p is the particle diameter, C_s is the slip correction factor, and μ is the gas viscosity.

The theory for large Reynolds number flow (potential flow with a boundary layer correction based on Hiemenz flow) past a flat disc was used to develop an expression for the gas velocity along the centerline. In dimensionless terms, the expression used is:

$$V_g^* = -1 : \text{for } -V_g^* \geq 1 \quad (14a)$$

$$V_g^* = -C\left[1 - 2/\pi\left(\tan^{-1}(1/z^*) - z^*/(z^{*2}+1)\right)\right] f(\eta)/\eta : \text{for } -V_g^* < 1 \quad (14b)$$

where $z^* = z/a_{eff}$ is the nondimensional distance above the target, and $f(\eta)/\eta$ is the boundary layer correction factor (White, 1974) with $\eta = (4\rho_g C a V_g^{\circ}/\pi\mu)^{1/2} z^*$. For convenience in evaluating the boundary layer correction factor, the numerical solution for $f(\eta)/\eta$ was fitted to within 1% by expressions of the form:

$$f(\eta)/\eta = 1 - \exp(-0.4722\eta) : \text{for } \eta < 2.2 \quad (15a)$$

$$f(\eta)/\eta = 1 - 0.80455/\eta : \text{for } \eta \geq 2.2 \quad (15b)$$

The expression for gas velocity contains two empirical parameters C, a correction factor, and a_{eff}, a vertical length scaling dimension. These constants were determined by applying the equation of motion to fit the trajectory data for 0.516-μm tracer particles. For

all impaction targets and nozzle flow rates, C was found to be $1.10 \pm 5\%$, and a_{eff} was 940 ± 20 μm, the latter corresponding closely to the 1000 μm diameter of the acceleration nozzle. As shown in Figure 7, the calculated trajectory for the tracer particles is in good agreement with the experimental points. The tracer particle velocity was very close to the centerline gas velocity, due to the small inertia of these 0.516-μm particles, which provided a sensitive test of the flow field expression.

Particle bounce was simulated by choosing a rebound velocity and calculating the corresponding particle rebound trajectory. The *rebound* velocity at the surface could then be determined to within a few percent by selecting the calculated trajectory that provided the best overall fit of the rebound velocity measurements.

In Figure 7, both primary and secondary impact trajectories are shown for 4.90-μm particles. Secondary impacts were especially useful in extending the investigation to lower impact velocities than were achievable for a single bounce event with the modified acceleration nozzle.

RESULTS

High-Velocity Impact

The ratios of rebound to impact velocities measured for 4.90-μm ammonium fluorescein particles over a wide range of impact velocities are shown in Figure 8 for four different targets. The velocity ratios increased strongly from the lowest impact velocities to maximum values as high as 0.85 at velocities near 20 m/s. At impact velocities < 20 m/s, a difference in the velocity ratio for a fixed impact velocity was observed for different target materials. For velocities > 40 m/s, the velocity ratio decreases with $< 5\%$ variation in impact energy loss between different targets. At the highest velocity, near 100 m/s, over 60% of the incoming energy was lost in the impact

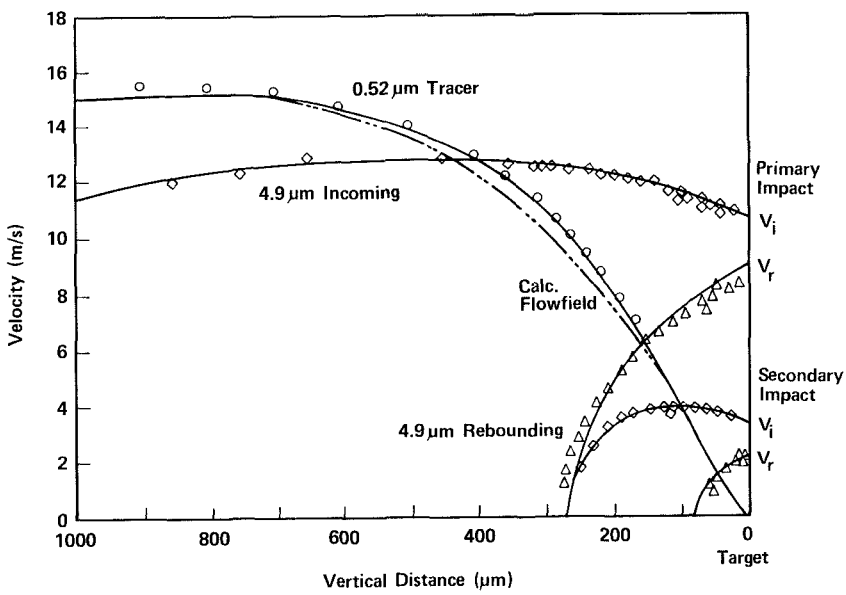

FIGURE 7. Velocity measurements for 4.90-μm particles showing trajectory fits for both primary and secondary bounces and the 0.52-μm tracer measurements used to establish the flowfield for the trajectory calculations.

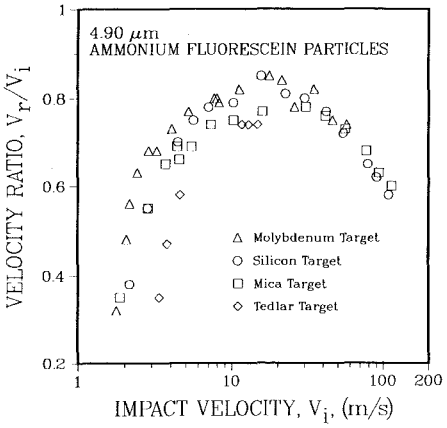

FIGURE 8. Velocity ratio (V_r/V_i) measurements over a full range of impact velocities (V_i) showing a dependence on target materials at low velocity and a lack of dependence at high velocity.

for both of the targets measured. These results can be understood qualitatively by applying the energy balance of Eq. (1). At sufficiently high velocity the impact energy, K_i, far exceeds the adhesion energy of the surface, ΔE, and the velocity ratio is primarily a function of the energy loss due to plastic deformation, which can be expressed as:

$$V_r/V_i = \left(1 - K_p/K_i\right)^{1/2} \simeq \left[1.94V_y/V_i - 0.88V_y^2/V_i^2\right]^{1/2} \quad (16)$$

by utilizing Eq. (4).

Accordingly, the velocity ratio decreases with increasing impact velocity. It is a function only of the elastic yield limit velocity and is independent of particle size. The small difference in velocity ratio observed between the different targets at high velocity indicates the elastic yield limit velocity was the same in each case, consistent with mechanical damage occurring only in the particle, which is believed to have a lower elastic yield limit than the target materials molybdenum, silicon, and mica. A similar decreasing trend in velocity ratio was reported by Dahneke for polystyrene microspheres impacting polished quartz at velocities above 35 m/s, also attributed to plastic deformation in the particle.

Low-Velocity Impact

In the low velocity impact range the energy loss is a function of the target material due to the adhesion surface energy which depends on the surface composition. The largest differences occurred near 3 m/s where the energy recovered (V_r^2/V_i^2) for a molybdenum target was 50% higher than for the mica and silicon targets, and 3.8 times higher than for the Tedlar target. The velocity ratio results for low velocity (< 20 m/s) impacts of different sizes of ammonium fluorescein particles with the four target materials are shown in Figures 9 and 10. Measurements were restricted by experimental constraints to particle sizes between 2 and 7 μm. Particles larger than 7 μm had

FIGURE 9. (*a*) Velocity ratio for low velocity impacts of different size particles with the molybdenum target, and (*b*) the fluorocarbon polymer target (Tedlar), with the energy balance equation fit to the measurements (*lines*).

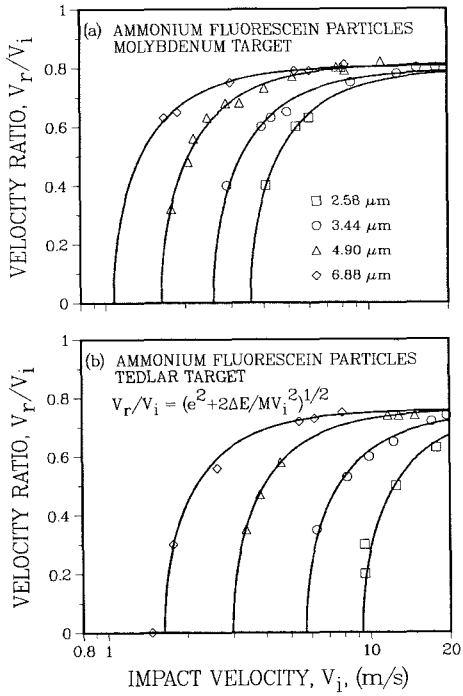

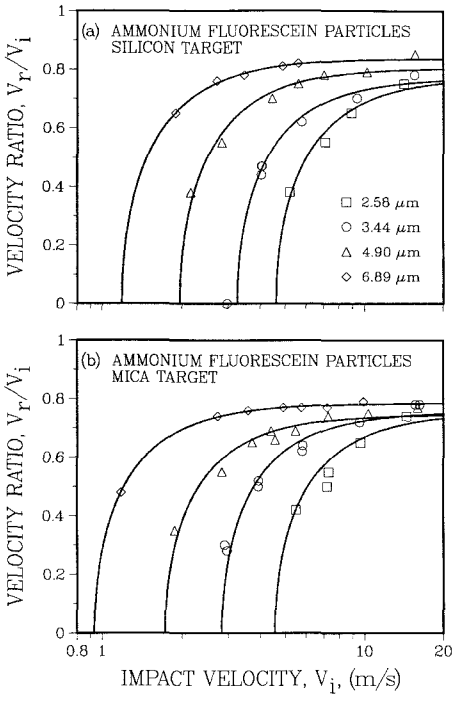

FIGURE 10. (*a*) Velocity ratio at low-impact velocity for different size particles impacting the polished silicon target and (*b*) the molecularly smooth mica target.

critical velocities less than 1 m/s, which were too low to be reproducibly achieved with the current nozzle. Particles smaller than 2 μm scattered insufficient light to be accurately detected close to the surface where they underwent very strong deceleration. This made velocity extrapolation to the impact surface uncertain.

In general, the velocity ratio decreased with decreasing impact velocity. Results for the two targets with the greatest difference in material characteristics are shown in Figure 9*a* and *b*. Molybdenum is a hard metal and Tedlar is a deformable fluorocarbon polymer; the two targets had a comparable degree of surface roughness. The experimental points were fit by using the simple two parameter (ΔE, e) energy balance [Eq. (1)], which gave an adequate representation of the data for impacts less than 20 m/s. Critical velocities were determined by extrapolation of the energy balance equation to zero rebound velocity [Eq. (2)]. Critical velocities for rebound increased with decreasing particle size, ranging from 1.1 m/s (with $d_p = 6.89$ μm) to 3.6 m/s (with $d_p = 2.58$ μm) for molybdenum, but were significantly higher, from 1.6 to 9.6 m/s, for Tedlar. A comparison of critical velocities and the fitting parameters for both targets at each particle size is included in Table 1.

The coefficient of restitution of near 0.8 observed for molybdenum, corresponding to a 40% energy loss, occurred at intermediate velocities where plastic damage begins to dominate the impact. The fraction of energy loss observed for all of the hard target materials was nearly the same, which is consistent with mechanical damage occurring only in the particles. A somewhat larger energy loss, near 50% ($e \simeq 0.7$), was observed for the Tedlar target, suggesting that plastic deformation may have also occurred in the foil. Similar coefficients of restitution were reported by Paw U (1983) for impacts of relatively smooth spores with a glass target ($e = 0.83$) and glass microspheres with natural leaf surfaces ($e = 0.76$–0.83). In each case the deformation would be expected to occur in the organic material. For organic particles, a coefficient of restitution > 0.90 has been reported by Dahneke (1975), and by Hays and Wayman (1983) for polystyrene latex microspheres striking a hard target under vacuum ($\leq 10^{-4}$ mm Hg). Some uncertainty in the composition of the surface layers of the polystyrene exists due to contamination from the chemical agents used to prevent coagulation of the microspheres during storage in water solution.

The low-velocity results for targets of silicon, the hard target with the best surface polish, and natural muscovite mica, having a molecularly smooth surface, are shown in Figure 10. Critical velocities for particles striking silicon and mica were intermediate between the results for molybdenum and Tedlar. The silicon and mica targets had

TABLE 1. Energy Balance Equation Fitting Parameters and the Calculated Critical Limits for Ammonium Fluorescein Particles Impacting Various Targets

Target material	Particle diameter (μm)	Adhesion energy $\lvert E_i - E_r \rvert$ (10^{-7} μJ)	Coefficient of restitution e	Critical velocity V_i^* (m/s)	Critical energy E_i^* (10^{-7} μJ)
Molybdenum	2.58	0.49	0.80	3.55	0.77
	3.44	0.60	0.80	2.56	0.94
	4.90	0.73	0.81	1.63	1.10
	6.89	0.87	0.81	1.07	1.33
Silicon	2.58	0.78	0.77	4.63	1.31
	3.44	0.90	0.77	3.25	1.52
	4.90	1.03	0.81	1.96	1.60
	6.89	1.13	0.84	1.18	1.62
Mica	2.58	0.71	0.75	4.55	1.26
	3.44	0.66	0.76	2.83	1.16
/^{210}Po	3.44	0.63	0.76	2.74	1.08
	4.90	0.69	0.75	1.72	1.23
	6.89	0.62	0.78	0.93	1.00
Tedlar	2.58	3.31	0.73	9.60	5.61
	3.44	2.65	0.75	5.69	4.66
	4.90	2.13	0.76	2.96	3.67
/gold	4.90	1.75	0.75	2.72	3.08
	6.89	1.78	0.76	1.64	3.09

similar critical velocities for large particles but the stronger particle size dependence with the mica target resulted in a smaller critical velocity for the smallest particles. Values for the critical velocity and the coefficient of restitution are included in Table 1 for each particle size and target material.

Electrostatic Effects

Since three of the four targets used were nonconductors, there was the possibility for accumulation of electrostatic charge on the surface which could affect the impact. Mica, which is commonly used as a dielectric material, was of special concern. Sufficient electrostatic charge buildup was normally present on the mica target to attract a 5-μm diameter glass fiber held near the surface, bending it to surface contact. Immediate release of the fiber occurred when a 500 μCi Po-210 source was placed within 0.5 cm of the target.

To evaluate the effect of electrostatic charge on rebound velocity, the velocity ratio for 4.9 μm ammonium fluorescein particles impacting the mica target was measured with and without continuous exposure to the ^{210}Po source. These data are shown in Figure 11*a*. Data for other target materials are also shown in order to illustrate the magnitude of any effect. The relatively small change in velocity ratio observed with and without surface discharge was less than the error in the velocity ratio measurements. This suggests that the electrostatic contribution to adhesion is not significant for these materials. Similar results were found when the same measurements were performed on the silicon target using the same size particles.

A lack of effect is also apparent from Figure 11*b*, for measurements on a Tedlar foil target with and without a thin gold coating applied to make the surface conducting. The coating provided a suitable electrostatic discharge path to ground, but was sufficiently thin (8.3 nm as determined by X-ray fluorescence analysis) to preserve the bulk mechanical properties of the Tedlar (Davies, 1949). The close agreement between velocity ratios for coated and un-

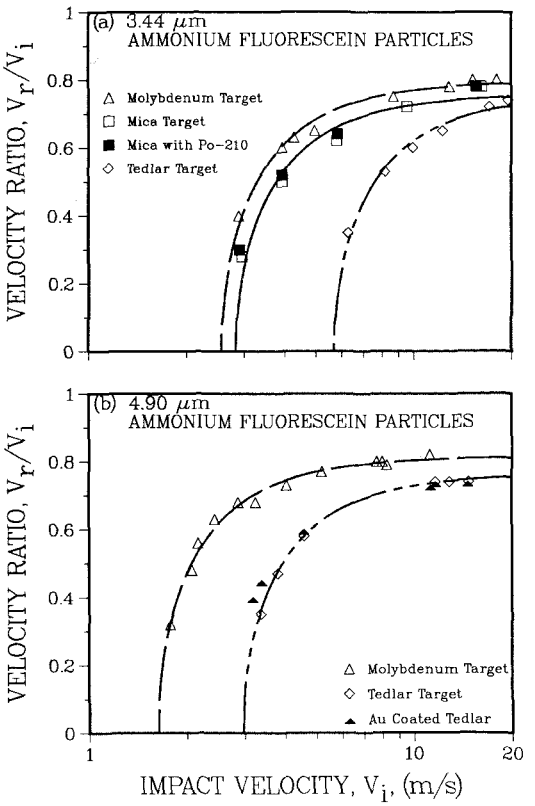

FIGURE 11. (*a*) A comparison of velocity ratios for impacts on the mica target with and without surface discharge with a ^{210}Po source. (*b*) The influence of a thin (8.3 nm) gold coating on the rebound velocity from the Tedlar target.

coated foils at the higher velocities, where some deformation is expected in the foil, is consistent with unaltered bulk properties.

The lack of appreciable change in the rebound velocity with the gold coating at low-impact velocity also suggests that the adhesion surface energy was similar for gold and Tedlar in our test environment. This seems unlikely for perfectly clean surfaces, since the adhesion surface energy of pure metals is appreciably higher than that for fluorocarbon polymers. However; this result is consistent with the presence of a layer of surface contamination which is known to form on metallic surfaces on exposure to room air (Fowkes, 1964).

Particle Size Dependence

In Figure 12 the energy ratio is plotted against the reciprocal of the impact energy for molybdenum and Tedlar, the targets with the greatest difference in material properties. An energy balance equation [essentially Eq. (1)] is fitted to the data for each particle size. Data points for impact velocities > 20 m/s, where e^2 decreases with increasing impact energy, are not included. The data for each target converge at the high energy end giving a y-intercept, e^2, nearly independent of particle size (see Table 1). Energy loss from mechanical damage appears to be greater in the Tedlar target (smaller value of e^2), than in the molybdenum target.

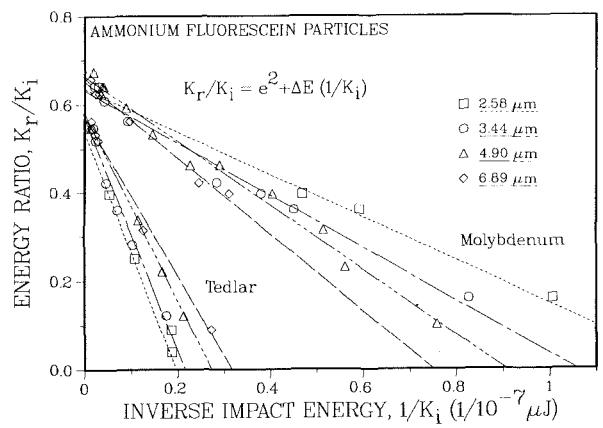

FIGURE 12. Fit to the data by a linearized plot of the energy balance equation.

The adhesion energy ΔE is obtained from the slope of a regression line through the data. The dependence of adhesion energy on particle size is evident for each target from the different slopes of the regression lines. However, the dependence on particle size is less than the difference between targets. The critical energy for rebound from the fluorocarbon polymer, Tedlar, was a factor of four higher than the $0.77–1.3 \times 10^{-7}$ μJ range determined for molybdenum.

The data for critical velocity as a function of particle size obtained in this study are plotted in Figure 13 with other relevant data from the literature for comparison. The absolute magnitudes of the present results are higher than the other reported measurements, probably because the present measurements were restricted to impacts in a narrow range around 90° to the surface. Wang and John (1988) found that at smaller angles of impact bounce can occur even if the normal component of velocity is below the critical velocity for 90° bounce. On the other hand, the slopes of the lines through the present results are in the same range as those of Wang and John (1988), Cheng and Yeh (1979), and D'Ottavio and Goren (1983) for impacts between organic particles and a harder surface material.

For a classical dispersion energy interaction between surfaces without deformation (Hamaker, 1937), a slope of -1 would be expected for all impact combinations. A less steep slope is predicted by the elastic flattening theory of Dahneke (1972). In general, all slopes for these widely different particle and surface combinations were significantly steeper than unity. A slope significantly less than unity occurred only for the results of Esmen. These measurements were unusual due to a coating of carbon on the impaction surface which was removed by the particles during impact. The steepest slopes were reported by Rogers and Reed (1984) for impacts between copper and harder materials.

In Figure 14, the critical velocity data collected in this study for impacts between ammonium fluorescein particles and the targets of molybdenum, silicon, Tedlar, and mica are plotted as a function of particle size. The data were fitted with the theory of Rogers and Reed (lines in Figure 14) using the criterion of Eq. (5) to determine the critical velocity for particles between 2 and 7 μm. The criterion was applied by assuming a mechanical constant κ and an elastic yield limit Y for the particle and varying the adhesion surface energy $\Delta\gamma$ to get a fit to the data. This process was repeated with adjusted values for κ and Y until fits of both molybdenum and silicon data could be obtained by changing only the adhesion surface energy. This assumes that deformation occurred only in the particle.

Table 2 shows the values obtained in each case using the model of Rogers and Reed. Although the mechanical constants are not known for ammonium fluorescein,

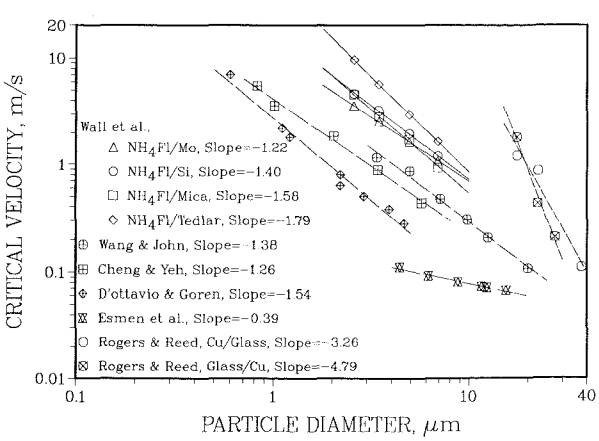

FIGURE 13. Comparison of available data relating critical velocity to particle size. NH_4Fl, ammonium fluorescein.

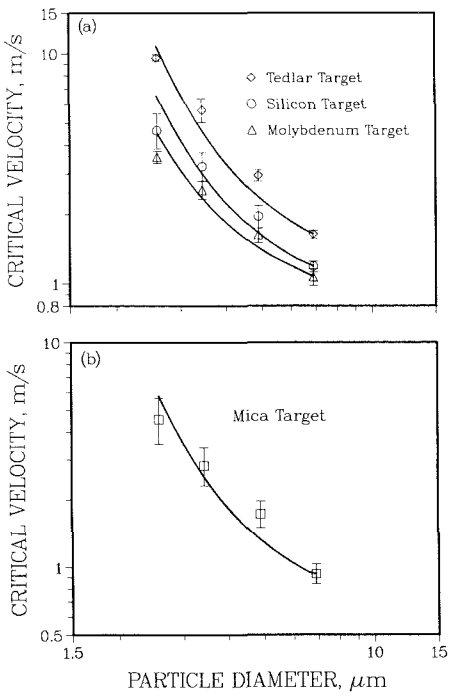

FIGURE 14. (*a*) Critical velocity vs. particle size for several target materials. The lines are fits to the data using the Rogers and Reed adhesion theory for elastic-plastic impacts. (*b*) Same as *a* for the mica target.

the values necessary to produce a fit of the data are within the range of properties found for other organic materials. For example, despite their very different chemical structures, the organic ring compounds cellulose acetate, styrene-polyester, butyl-polystyrene, and phenol-formaldehyde all have mechanical constants κ in the range $3\text{–}8 \times 10^{-10}$ m^2/N and elastic yield limits Y from $4\text{–}8 \times 10^7$ N/m^2, which encompass the values chosen for ammonium fluorescein. In the case of Tedlar, deformation apparently occurs in the target, since a fit of the data is obtained by using the values of the mechanical constant κ and the elastic yield stress Y for Tedlar, which are known from the manufacturer.

The adhesion surface energies obtained for impacts with the different target materials (Table 2) are larger than the range expected for the dispersion component of surface energy alone. The dispersive surface energy has been shown by Fowkes (1964) to be the sum of geometric mean of the surface energies of the materials:

$$\Delta\gamma = 2\left[\gamma_p^d \gamma_s^d\right]^{1/2}, \tag{17}$$

where γ_p^d and γ_s^d are the dispersive components of surface energy for the particle and the target. Dispersive surface energies for phenyl ring edge structures like polystyrene and ammonium fluorescein are in the range 0.04–0.05 J/m^2 as suggested by Zisman (1963) and as reported by Fowkes (1964) for several substituted aromatic hydrocarbons. For the transition metal molybdenum and nonmetallic silicon, values in the range 0.10–0.14 J/m^2 would be expected based on dispersion surface energies reported by Fowkes for several transition metals and metal oxides (titanium, iron, tin) and the 0.12 J/m^2 value determined for silicon ox-

TABLE 2. Fitting Parameters for the Critical Velocity Particle Size Dependence of Ammonium Fluorescein Particles Impacting Various Targets

Target material	Mechanical constant[a] κ_p (10^{-10} m^2/N)	κ_s (10^{-10} m^2/N)	Elastic yield limit Y (10^7 N/m^2)	Yielding material	Surface energy $\Delta\gamma$ (J/m^2)
Mica	7.6	0.100[1]	6.8	particle	0.28
Molybdenum	7.6	0.028[2]	7.4	particle	0.34
Silicon	7.6	0.050[3]	7.4	particle	0.38
Tedlar[b]	7.6	4.5[4]	5.8[4]	target	0.47

[a] $\kappa = (1-\nu^2)/\xi$; $\nu = 0.33$ and ξ was taken from the following sources:

1. Derjaguin, Muller, and Toporov (1980). *J. Colloid Interface Sci.* 1:293.
2. Gray, D. E. (ed.). (1972). *American Institute of Physics Handbook* McGraw-Hill, New York.
3. Gilman, J. J. (1960). *Appl. Phys.* 31:2208.
4. Manufacturer's data (Polymers Division, Dupont Co.)

[b] Polyvinylfluoride.

ides. The adhesion energies $\Delta\gamma$ calculated [Eq. (17)] from these estimates of the dispersive surface energy for the particle and target materials are in the range 0.13–0.17 J/m^2, which is considerably lower than the fitted values determined for both molybdenum and silicon (0.34, and 0.38 J/m^2). Rogers and Reed (1984) reported a similar disagreement between the dispersive surface energy determined from liquid contact angle measurements on copper and glass (0.12–0.14 J/m^2), and the higher range of values estimated from critical velocities for particle-surface impacts between these materials (0.18–0.25 J/m^2).

The energy loss due to plastic damage in the annular region under tension at the perimeter of the contact area was evaluated with the model of Fichman and Pnueli (1985) using the material constants for mica and ammonium fluorescein from Table 2. Application of the model followed the assumption of Fichman and Pnueli (1986), that only the energy dissipated at the perimeter of the contact circle, K_{p2}, is required to determine the critical impact velocity below which particles stick to a surface. Accordingly, the critical velocity was simply calculated as $V_i^* = (2K_{p2}/M)^{1/2}$.

Applied in this fashion, without considering plastic deformation at the center of the contact circle or the adhesion energy which acts over an entire contact area, the Fichman and Pnueli model greatly underestimates the magnitude and the particle size dependence of the critical velocity. For completeness, the plastic deformation energy losses from both the contact perimeter and center of the contact circle areas should be included in the theory. Unfortunately the energy losses from the models of Rogers and Reed, and Fichman and Pnueli cannot simply be added together since the two effects are not independent during the impact.

An apparent overestimate of the adhesion surface energy obtained from fits of the Rogers and Reed model to the data is consistent with 1) an underestimation of the maximum contact area which results from the assumption that equilibrium between stored elastic and lost surface energy is achieved during the impact, 2) an underestimate of the actual surface energy by not considering the contribution of nondispersive components in calculating the adhesion surface energy, and 3) a failure to account for additional energy losses including plastic damage at the contact perimeter which is under tension from surface forces, and kinetic materials effects such as viscoelastic energy dissipation at the contact perimeter and in the bulk material.

Points 1 and 3 are defects in the model which are discussed further in the next section. Regarding point 2, the total adhesion surface energy (Dupré work of adhesion) can also include a contribution from polar interactions in addition to the dispersion interaction which is always present. Ammonium fluorescein is a multiring aromatic hydrocarbon with polar hydroxyl functional groups and an ionicly bonded ammonium group which can form particularly strong hydrogen bonds with polar oxide surfaces. For ammonium fluorescein in contact with the molybdenum and silicon targets, the polar contribution to surface energy would be expected to be less than the dispersion component as has been suggested by Fowkes for highly polar organic materials in general. Therefore, even including the polar contribution, the total surface energy would be significantly less than the fitted values from the impact measurements. Direct measurements of the adhesion energy of a mica surface exposed to air range from 0.25 J/m^2 for an aged surface to 0.38 J/m^2 for a fresh surface as reported by Bowden (1962). The fitted value, 0.29 J/m^2, lies in this range.

No direct measurements of the dispersion component of surface energy are available for Tedlar. Estimates of surface energies for fluorocarbon polymers range from < 0.036 J/m^2 for crystallization in air to > 0.07 J/m^2 for crystallization in contact with a metal surface. A much larger adhesion surface energy of over 0.40 J/m^2 is

required to fit the Tedlar target impact data with the theoretical model. This is considerably larger than the adhesion surface energy of any of the hard targets. Kendall (1974) and later Johnson (1976) have attributed the large apparent adhesion surface energy observed for other elastomers to kinetic effects which include viscoelastic energy dissipation at the contact margin.

ADHESION MODELS FOR IMPACT

Few adhesion models for impacts have been developed which include the complexities of both plastic and elastic deformation. The currently available models include assumptions which are introduced to simplify the interaction between the mechanical and adhesion forces which occur throughout the impact. In the adhesion model for elastic-plastic impacts presented by Rogers and Reed the adhesion energy is neglected in the compressive (incoming) phase of the impact during which the maximum contact area is achieved. At the end of the incoming phase the Johnson, Kendell, and Roberts (JKR) theory for *equilibrium* is applied to determine the adhesion energy. Accordingly, this assumption applied to the dynamic impact underestimates the contact area. An underestimate in the contact area would require an overestimate of specific adhesion surface energy to fit the theory to the data, as was observed. Additional energy losses which are not considered are the plastic damage at the edge of the contact area which is under tension, and the enhancement of the plastic damage at the center of contact due to the action of the adhesion force during compression.

The Rogers and Reed theory assumes a constant yield limit stress, which produces increasingly larger overestimates of the energy loss as impacts occur further above the critical velocity. Recently Wall et al. (1989) utilized a dynamic yield limit function fit to the laser-Doppler data in order to modify the Rogers and Reed model. The modified model agreed well with the experimental measurements over the entire impact velocity range from 1 to 100 m/s. However, the required surface energy parameters remain unrealistically large.

Fichman and Pnueli calculate the kinetic energy, including the contribution from the attractive surface forces which is required to reach the elastic yield limit at the center of contact. However, the elastic energy stored after the yield limit is reached is not considered and all the excess energy is assumed to be lost to plastic damage. No method for calculating plastic damage at the center of contact is given; rather, critical velocity is calculated from the energy loss which is considered to occur in the ring of plastic deformation at the edge of contact area, where the material is in tension. The JKR theory is used in the equations of motion with the assumption that the static theory applies, which is not appropriate since equilibrium is not achieved during the impact motion. As with Rogers and Reed, the adhesion energy will be underestimated since the motion overshoots the equilibrium point. Even when numerous errors in the equations are corrected, the model of Fichman and Pnueli greatly under estimates the critical velocity for particle bounce and the associated dependence on particle size.

CONCLUSIONS

A laser Doppler velocimetry system has been developed for measuring incoming and rebounding particle velocities to within several particle diameters of the impaction surface. At low velocity (< 20 m/s), the ratio of rebound to impact velocity was sensitive to target material, decreasing with impact velocity due to the adhesion surface energy. The kinetic energy recovered in low velocity impacts was found to depend on particle size. No such particle size dependence was observed for impact velocities near 20 m/s, consistent with expectations for plastic deformation. Above 40 m/s, the velocity ratio was insensitive to the target material, indicating that the particle has a lower elastic yield limit than molybdenum, silicon, or mica. Plastic deformation was a significant

component of energy loss at all impact velocities investigated.

Critical velocities for the initiation of bounce were found to decrease with a stronger power-law dependence on particle diameter than expected from classical adhesion theory, the elastic flattening model proposed by Dahneke, or the adhesion-induced plastic damage approach of Fichman and Pnueli. The critical particle size dependence can be fitted by the theory of Rogers and Reed (1984), consistent with a contribution to particle adhesion from both plastic deformation and surface energy; however, the required surface energy parameter is considerably higher than expected. There is currently no comprehensive theory for particle surface impacts which incorporates all the components of energy loss. A dynamic theory is required which includes surface forces throughout the impact, and which accounts for the energy loss to plastic deformation under compression at the center of contact and under tension at the contact perimeter.

Auxiliary experiments were conducted with continuous discharging of the mica impaction surface by a ^{210}Po alpha source and with a Tedlar target coated with a thin layer of gold to make it conducting. The results indicated the absence of a significant contribution to particle adhesion from electrostatic charge.

Dr. Helmut Mothes participated in the early phases of this work and made valuable contributions to the development of the experimental technique. This work was supported by the National Science Foundation Grant Nos. CBT-8442795 and CPE-8103635.

REFERENCES

Aylor, D. E., and Ferrandino, F. J. (1985). *Atmos. Environ.* 5:803–806.

Bitter, J. G. A. (1963). *Wear* 6:5–21.

Brenner, S. S., Wrient, H. A., and Oriani, R. A. (1981). *Wear* 68:169–190.

Bowden, F. P. (1962). In *Adhesion and Cohesion* (P. Weiss, ed.). Elsevier, New York.

Broom, G. P. (1979). *Filtrat. Sep.* Nov./Dec.

Cheng, Y. S., and Yeh, H. C. (1979). *Environ. Sci. Technol.* 13:1392–1396.

Dahneke, B. (1971). *J. Colloid Interface Sci.* 37:342–353.

Dahneke, B. (1972). *J. Colloid Interface Sci.* 40:1–13.

Dahneke, B. (1973). *J. Colloid Interface Sci.* 45:584–590.

Dahneke, B. (1975). *J. Colloid Interface Sci.* 51:58–65.

Davies, R. M. (1949). *Proc. R. Soc.* A 197:417–432.

D'Ottavio, T., and Goren, S. L. (1983). *Aerosol. Sci. Technol.* 2:91–108.

Drain, L. E. (1972). *J. Phys. D Appl. Phys.* 5:481–495.

Esmen, N. A., Ziegler, P., and Whitfield R. (1978). *J. Aerosol Sci.* 9:547–556.

Fichman, M., and Pnueli, D. (1985). *J. Appl. Mech.* 52:105–108.

Fichman, M., and Pnueli, D. (1986). *J. Appl. Mech.* 53:230–231.

Fowkes, F. M. (1964). *Ind. Eng. Chem.* 56:40–52.

Hamaker, A. C. (1937). *Physica* 4:1058.

Hays, D. A., and Waymam W. H. (1983). *Adhesion of Charged Particles*. Institute of Physics Conference Serial No. 66.

Hiller, R. and Löffler, F. (1980). *Ger. Chem. Eng.* 3:327–332.

John, W., and Wall, S. M. (1983) *J. Aerosol Sci.* 14:713–727.

Johnson, K. L. (1976). In *Theoretical and Applied Mechanics*. (W. T. Koiter, ed.). North-Holland, New York.

Johnson, K. L., Kendall, K., and Roberts, A. D. (1971). *Proc. R. Soc. Lond.* 324:301–313.

Kendall, K. (1974). *J. Adhes.* 7:55–72.

Paw U. K. T. (1983). *J. Colloid Interface Sci.* 93:442–452.

Reed, J. (1986). *J. Appl. Mech.* 53:229–230.

Rogers, L. N., and Reed, J. (1984). *J. Phys. D Appl. Phys.* 17:677–689.

Tabor, D. (1977). *J. Colloid Interface Sci.* 58:2–13.

Timoshenko, S., and Goodier, J. N. (1951). *Theory of Elasticity*, 2nd ed. McGraw-Hill, New York.

Vanderpool, R. W., and Rubow, K. L. (1984). *TSI Q.* Jan./Mar.

Wall, S. M., John, W., and Rogers, D. (1985). *Aerosol Sci. Technol.* 4:81–87.

Wall, S. M., John, W., and Goren S. L. (1989). In *Particles on Surfaces 2: Detection, Adhesion and Removal* Edited by K. L. Mittal. Plenum Press, New York.

Wang, H. C., and John, W. (1988). In *Particles on Surfaces 1: Detection, Adhesion and Removal* Edited by K. L. Mittal. Plenum Press, New York.

White, F. M. (1974). *Viscous Fluid Flow*. McGraw-Hill, New York, Chapter 3.

Zisman, W. A. (1963). *Ind. Eng. Chem.* 55:19–38.

Received July 13, 1988; accepted January 31, 1989.